High-angular-momentum topological superconductivities in twisted bilayer quasicrystal systems

Yu-Bo Liu,[1,*] Yongyou Zhang,[1,*] Wei-Qiang Chen,[2,3,†] and Fan Yang[1,‡]
[1]*School of Physics, Beijing Institute of Technology, Beijing 100081, China*
[2]*Department of Physics and Shenzhen Institute for Quantum Science and Engineering, Southern University of Science and Technology, Shenzhen 518055, China*
[3]*Shenzhen Key Laboratory of Advanced Quantum Functional Materials and Devices, Southern University of Science and Technology, Shenzhen 518055, China*

(Received 25 January 2022; revised 10 November 2022; accepted 20 December 2022; published 4 January 2023)

The electron states in the quasicrystal (QC) are hot topics recently. While previous attentions were focused on such intrinsic QCs as the Penrose lattice, the recent "*twistronics*" provides us with a new type of QC, i.e., the extrinsic QC, including the 30°-twisted bilayer graphene and 45°-twisted bilayer cuprates as two synthesized examples, unifiedly dubbed as TB-QC. Here we build an efficient microscopic framework to study electron-electron interaction driven superconductivities (SCs) in these extrinsic QCs, and find that their nature sits in between those of crystals and intrinsic QCs. Remarkably, our microscopic calculations on the three exemplar TB-QCs reveal various novel topological SCs carrying high angular momenta and high Chern numbers protected by their unique QC symmetries, absent in conventional crystalline materials. The nature of SCs in these extrinsic QCs is also fundamentally different from those in intrinsic QCs in the aspect of pairing-symmetry classifications and topological properties.

DOI: 10.1103/PhysRevB.107.014501

I. INTRODUCTION

The quasicrystal (QC) indicates a special type of structure which hosts long-range order and rotation symmetry, but lacks of translation period [1,2]. Presently, most studies in this area [3–34] were performed on intrinsic QCs such as the Penrose lattice, which hosts the quasiperiodic nature by itself. On the other front, the rapid development of the "*twistronics*" [35–81] provides us with another type of QC, i.e., the extrinsic QC, made through stacking two identical crystalline monolayers with the largest possible twist angle [82–88], dubbed as the twisted bilayer QC (TB-QC) here. Synthesized examples of TB-QC include the 30°-twisted bilayer graphene [82–86] and the 45°-twisted bilayer cuprates [87,88]. Different from intrinsic QCs, the structure of TB-QCs is periodic within each monolayer, and the quasiperiodic nature appears only in the perturbational coupling between the two layers. Since the structures of TB-QCs sit in between those of crystals and intrinsic QCs, one might conjecture that the physical properties of TB-QCs should also sit in between them in some sense. The single-particle properties of some TB-QCs have been investigated [82,83,89–93], and such intriguing states as the 12-fold resonant spatially localized states have been revealed [89]. However, the electron-electron (e-e) interaction driven properties in the TB-QCs have not been microscopically investigated.

In this paper, we build an efficient microscopic framework based on a revised version of the perturbational-band theory [82,83,94,95], to study e-e interaction driven instabilities in extrinsic QCs, with a focus on possible topological superconductivities (TSCs) in the TB-QCs. Our **k**-space approach enables examination of the distribution of the pairing gap function on the Fermi surface (FS), and thus is more convenient and intuitive than real-space approaches in the studies of the pairing symmetries and topological properties. A classification of the pairing symmetries suggests that, due to the doubly enlarged rotation symmetry group relative to its monolayer, various high-angular-momentum (HAM) TSCs absent in conventional crystalline materials can emerge in the TB-QCs. In short, as a crystal can host at most sixfold rotation axes, only the $p+ip$ or $d+id$ TSCs with pairing angular momentum $L=1$ or $L=2$ are allowed by the symmetry; while the three exemplar TB-QCs studied here exhibit novel $g+ig$- ($L=4$), $h+ih$- ($L=5$) and $d+id$- TSCs respectively, as revealed by our microscopic calculations. In the aspect of topology, these HAM TSCs are associated with higher Chern numbers than twice of those realized in each monolayer, due to a FS reconstruction caused by the interlayer coupling. The pairing-symmetry classification and the topological properties of these TSCs are also fundamentally different from those in intrinsic QCs. Our microscopic framework can also be used to study other electron instabilities in extrinsic QCs.

The following parts of the paper are organized as follow. In Sec. II, we provide our microscopic framework for the succeeding studies. In Sec. III, a pairing-symmetry classification is performed based on irreducible representations (IRRPs) of the point group. In Sec. IV, we provide the results of our systematic microscopic calculations on the three exemplar systems, including the 30°-twisted bilayer graphene, the 30°-twisted bilayer BC_3 and the 45°-twisted bilayer cuprates. In Sec. V, we study the topological properties of the HAM

*These authors contributed equally to this work.
†chenwq@sustech.edu.cn
‡yangfan_blg@bit.edu.cn

 ©2023 American Physical Society

TSCs obtained by our microscopic calculations. In Sec. VI, we arrive at our conclusion after some discussions.

II. MICROSCOPIC FRAMEWORK

The tight-binding (TB) Hamiltonians of the TB-QCs studied here take the real-space single-orbital form of

$$H_{\rm TB} = \sum_{\mathbf{ij}\sigma} t_{\mathbf{ij}} c^{\dagger}_{\mathbf{i}\sigma} c_{\mathbf{j}\sigma}. \tag{1}$$

Here σ labels spin and $t_{\mathbf{ij}}$ represents the hopping integral between the sites $\mathbf{i}$ and $\mathbf{j}$ which can locate in either the same or different layers. The concrete formula of $t_{\mathbf{ij}}$ for the interlayer hopping is given as [89]

$$t_{\mathbf{ij}} = t_{\mathbf{ij}\pi}\left[1 - \left(\frac{\mathbf{R_{ij}}\cdot\mathbf{e_z}}{R}\right)^2\right] + t_{\mathbf{ij}\sigma}\left(\frac{\mathbf{R_{ij}}\cdot\mathbf{e_z}}{R}\right)^2, \tag{2}$$

with

$$t_{\mathbf{ij}\pi} = t_\pi e^{-(R_{\mathbf{ij}}-a)/r_0}, \quad t_{\mathbf{ij}\sigma} = t_\sigma e^{-(R_{\mathbf{ij}}-d)/r_0}.$$

Here, $R_{\mathbf{ij}}$ is the length of the 3D vector $\mathbf{R_{ij}}$ pointing from $\mathbf{i}$ to $\mathbf{j}$, and $\mathbf{e_z}$ is the unit vector perpendicular to the layer. The parameters $a, d, r_0, t_\pi, t_\sigma$ denote the lattice constant, interlayer spacing, normalization distance, in-plane hoping, and vertical hoping, respectively. These parameters for the three exemplar systems are given separately in the following. The formulas of intralayer hopping integrals for the three exemplar systems are also provided separately below.

As treated in the perturbational-band theory [82,83,94,95], this Hamiltonian is decomposed into the zeroth-order intralayer hopping term H_0 and perturbational interlayer tunneling term H' as

$$H_0 = \sum_{\mathbf{k}\mu\alpha\sigma} c^{\dagger}_{\mathbf{k}\mu\alpha\sigma} c_{\mathbf{k}\mu\alpha\sigma} \varepsilon^{\mu\alpha}_{\mathbf{k}},$$
$$H' = \sum_{\mathbf{kq}\alpha\beta\sigma} c^{\dagger}_{\mathbf{k}\mathrm{t}\alpha\sigma} c_{\mathbf{q}\mathrm{b}\beta\sigma} T^{\alpha\beta}_{\mathbf{kq}} + \mathrm{H.c.} \tag{3}$$

Here, $\mathbf{k}/\mathbf{q}$, μ [= t (top), b (bottom)], and α/β label the momentum, layer, and band, respectively. $\varepsilon^{\mu\alpha}_{\mathbf{k}}$ is the monolayer dispersion and the tunneling matrix element $T^{\alpha\beta}_{\mathbf{kq}}$ is given by [52,94,95]

$$T^{\alpha\beta}_{\mathbf{kq}} = \langle \mathbf{k}\alpha^{(\mathrm{t})} | H_{\rm TB} | \mathbf{q}\beta^{(\mathrm{b})} \rangle. \tag{4}$$

Here $|\mathbf{k}\alpha^{(\mu)}\rangle$ represents a monolayer state on the layer μ, which is an eigenstate of H_0. In thermal dynamic limit, the nonzero $T^{\alpha\beta}_{\mathbf{kq}}$ requires the revised momentum-conservation condition $\mathbf{k} + \mathbf{G}^{(\mathrm{t})} = \mathbf{q} + \mathbf{G}^{(\mathrm{b})}$ [82,83,94,95]. Here $\mathbf{G}^{(\mathrm{t/b})}$ represent the reciprocal lattice vectors for the t/b layers. Under this condition, we have $T^{\alpha\beta}_{\mathbf{kq}} \propto t(\mathbf{k} + \mathbf{G}^{(\mathrm{t})})$, which decays promptly with $|\mathbf{k} + \mathbf{G}^{(\mathrm{t})}|$ [82,83,94,95]. Therefore each top-layer eigenstate $|\mathbf{k}\alpha^{(\mathrm{t})}\rangle$ can only couple with a few isolated bottom-layer eigenstates $|\mathbf{q}\beta^{(\mathrm{b})}\rangle$, and vice versa, which justifies the perturbational treatment of the interlayer coupling.

To build a framework convenient for involving local e-e interactions in the TB-QCs, one should start from a finite lattice, on which the revised momentum-conservation condition cannot be exactly satisfied between the two mutually incommensurate sets of momenta points on the two layers. Therefore, for each top-layer state $|\mathbf{k}\alpha^{(\mathrm{t})}\rangle$, we ignore this condition and directly use Eq. (4) to find the bottom-layer states $|\mathbf{q}_i\beta^{(\mathrm{b})}_i\rangle$ which obviously couple with it. Then, for these $|\mathbf{q}_i\beta^{(\mathrm{b})}_i\rangle$ states, we find again all the $|\mathbf{k}'_j\alpha^{(\mathrm{t})}_j\rangle$ states which obviously couple with them. Gathering all these states related to $|\mathbf{k}\alpha^{(\mathrm{t})}\rangle$ as bases to form a close sub-space, we can diagonalize the Hamiltonian matrix in this subspace to obtain all the eigenstates. Among these states, the one having the largest overlap with $|\mathbf{k}\alpha^{(\mathrm{t})}\rangle$ is marked as its perturbation-corrected state $|\widetilde{\mathbf{k}\alpha^{(\mathrm{t})}}\rangle$, whose energy is marked as $\tilde{\varepsilon}^{\mathrm{t}\alpha}_{\mathbf{k}}$. Similarly, we get $|\widetilde{\mathbf{q}\beta^{(\mathrm{b})}}\rangle$ and $\tilde{\varepsilon}^{\mathrm{b}\beta}_{\mathbf{q}}$. We have checked that different $|\widetilde{\mathbf{k}\alpha^{(\mu)}}\rangle$ thus obtained are almost mutually orthogonal, qualifying $\{|\widetilde{\mathbf{k}\alpha^{(\mu)}}\rangle\}$ as a good set of single-particle bases, in which the TB Hamiltonian can be diagonalized as

$$H_{\rm TB} = \sum_{\mathbf{k}\mu\alpha\sigma} \tilde{\varepsilon}^{\mu\alpha}_{\mathbf{k}} \tilde{c}^{\dagger}_{\mathbf{k}\mu\alpha\sigma} \tilde{c}_{\mathbf{k}\mu\alpha\sigma}. \tag{5}$$

Here the operator $\tilde{c}^{\dagger}_{\mathbf{k}\mu\alpha\sigma}$ ($\tilde{c}_{\mathbf{k}\mu\alpha\sigma}$) creates (annihilates) the eigenstate $|\widetilde{\mathbf{k}\alpha^{(\mu)}}\rangle$ with spin σ.

The set of dispersion relation $\tilde{\varepsilon}^{\mu\alpha}_{\mathbf{k}}$ defines a band structure, associated with a FS for a given filling fraction. It's remarkable that, despite the QC structure, there still can be well defined band structure and FS in the TB-QC, due to its weak interlayer coupling. What's more, the band structure and FS of a TB-QC can possess higher-fold rotation symmetry absent in a crystal. Let's take the 45°-twisted bilayer cuprates as an example. Figures 1(a) and 1(b) show the band structure and the associated quartic symmetric FS for $\delta = 0.1$ hole-doping of the separate bottom layer. Then the top layer is stacked above

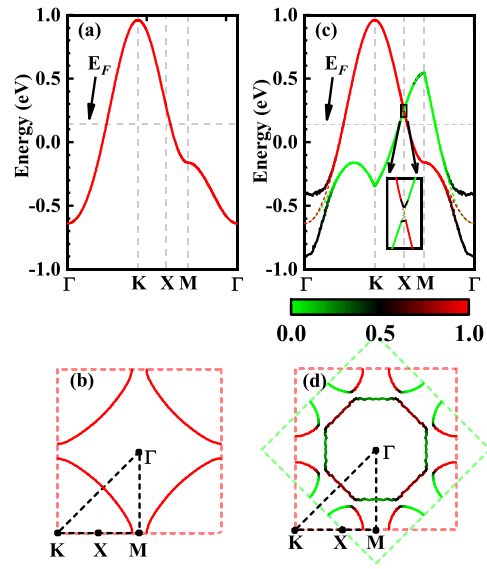

FIG. 1. (a) Band structure along the high-symmetry points and (b) FS for $\delta = 0.1$ hole doping of the cuprates monolayer. (c) Band structure and (d) FSs of the corresponding 45°-twisted bilayer. The colors in (c) and (d) represent layer component. The Fermi energy E_F is marked in (a) and (c). The inset of (c) exhibit the band splitting. In plotting (d), the interlayer coupling has been doubly enlarged to enhance the FS splitting so as to enhance the visibility.

TABLE I. IRRPs of D_{2n} and corresponding pairing-symmetry classification. The first column gives the names of the IRRPs. The second and third columns provide the matrix representations of the two generators, up to an arbitrary unitary transformation. In the fourth column, the basis function(s) of each IRRP is provided. In the fifth column, the symmetry-transformation properties of the ground-state gap function is given. Here $\hat{P}_\theta$ denotes the rotation by the angle $\theta = \frac{\pi}{n}$ about the z axis.

IRRPs		$D_{(C_{2n}^1)}$	$D_{(\sigma_y)}$	Basis functions	Ground-state gap functions
1D	A_1	I	I	1	$\hat{P}_\theta\Delta = \Delta, \hat{\sigma}_y\Delta = \Delta$
	A_2	I	$-I$	$(C_n^1 x^{n-1}y - C_n^3 x^{n-3}y^3 + \dots) * (x^n - C_n^2 x^{n-2}y^2 + \dots)$	$\hat{P}_\theta\Delta = \Delta, \hat{\sigma}_y\Delta = -\Delta$
	B_1	$-I$	I	$x^n - C_n^2 x^{n-2}y^2 + \dots$	$\hat{P}_\theta\Delta = -\Delta, \hat{\sigma}_y\Delta = \Delta$
	B_2	$-I$	$-I$	$C_n^1 x^{n-1}y - C_n^3 x^{n-3}y^3 + \dots$	$\hat{P}_\theta\Delta = -\Delta, \hat{\sigma}_y\Delta = -\Delta$
2D	E_1	$I\cos\frac{\pi}{n} - i\sigma_y\sin\frac{\pi}{n}$	σ_z	(x, y)	$\hat{P}_\theta\Delta = e^{\mp i\frac{\pi}{n}}\Delta, \hat{\sigma}_y\Delta = \Delta^*$
	…	…	…	…	…
	E_L	$I\cos\frac{L\pi}{n} - i\sigma_y\sin\frac{L\pi}{n}$	σ_z	$(x^L - C_L^2 x^{L-2}y^2 + \dots,\ C_L^1 x^{L-1}y - C_L^3 x^{L-3}y^3 + \dots)$	$\hat{P}_\theta\Delta = e^{\mp i\frac{L\pi}{n}}\Delta, \hat{\sigma}_y\Delta = \Delta^*$
	…	…	…	…	…
	E_{n-1}	$I\cos\frac{(n-1)\pi}{n} - i\sigma_y\sin\frac{(n-1)\pi}{n}$	σ_z	$(x^{n-1} - C_{n-1}^2 x^{n-3}y^2 + \dots, C_{n-1}^1 x^{n-2}y - C_{n-1}^3 x^{n-4}y^3 + \dots)$	$\hat{P}_\theta\Delta = e^{\mp i\frac{(n-1)\pi}{n}}\Delta, \hat{\sigma}_y\Delta = \Delta^*$

the bottom one with the relative twist angle 45°. In Fig. 1(c), the band structures of the separate top layer (green dashed), the separate bottom layer (red dashed) and the coupled bilayer (solid lines with the color changing with momentum, representing layer component) are laid together. The inset of (c) exhibits that, while the two uncoupled band structures cross at the X point (or more generally, the Γ-X lines), such band crossing is split upon the interlayer band hybridization, forming into two new coupled band structures. Meanwhile, the FSs from the two separate layers are 45°-rotation related and cross, which are split by the interlayer hybridization into two octagonal symmetric FSs, as shown in Fig. 1(d). The two new FSs can be viewed as the interlayer bonding and antibonding FSs. Such fascinating high-symmetric FSs are forbidden in conventional crystalline materials.

The above single-particle bases $\{|\widetilde{\mathbf{k}\alpha^{(\mu)}}\rangle\}$ provide us with an efficient framework to conveniently treat with the e-e interactions in the $\mathbf{k}$ space, using which we can study various instabilities. Here we focus on the SC. Concretely for a given system, the effective pairing interaction obtained in the real space is transformed to this $\mathbf{k}$-space bases. Considering only intraband pairing between opposite momenta, we get the following effective BCS Hamiltonian,

$$H_{\mathrm{BCS}} = H_{\mathrm{TB}} + \frac{1}{N}\sum_{\substack{\mathbf{k}\mu\alpha\\ \mathbf{q}\nu\beta}} \tilde{c}^\dagger_{\mathbf{k}\mu\alpha\downarrow}\tilde{c}^\dagger_{-\mathbf{k}\mu\alpha\uparrow}\tilde{c}_{-\mathbf{q}\nu\beta\uparrow}\tilde{c}_{\mathbf{q}\nu\beta\downarrow}V^{\mu\nu}_{\alpha\beta}(\mathbf{k},\mathbf{q}), \tag{6}$$

where $V^{\mu\nu}_{\alpha\beta}(\mathbf{k},\mathbf{q})$ is the effective pairing interaction. Under the mean-field (MF) treatment involving $\Delta_{\mu\alpha}(\mathbf{k}) \equiv \frac{1}{N}\sum_{\mathbf{q}\nu\beta} V^{\mu\nu}_{\alpha\beta}(\mathbf{k},\mathbf{q})\langle\tilde{c}_{-\mathbf{q}\nu\beta\uparrow}\tilde{c}_{\mathbf{q}\nu\beta\downarrow}\rangle$ as the pairing gap function, we obtain the following linearized gap equation near the superconducting T_c [96]:

$$-\frac{1}{(2\pi)^2}\sum_{\nu\beta}\oint dq_\parallel \frac{V^{\mu\nu}_{\alpha\beta}(\mathbf{k},\mathbf{q})}{v_F^{\nu\beta}(\mathbf{q})}\Delta_{\nu\beta}(\mathbf{q}) = \lambda\Delta_{\mu\alpha}(\mathbf{k}). \tag{7}$$

This equation is solved to yield the largest pairing eigenvalue λ and corresponding eigenvector $\Delta_{\mu\alpha}(\mathbf{k})$. The former and latter determine the T_c and the gap function respectively.

Under this framework, we study the pairing states in three examples, including the 30°-twisted bilayer graphene, 30°-twisted bilayer BC_3 and 45°-twisted bilayer cuprates. For the 30°-twisted bilayer graphene and 45°-twisted bilayer cuprates with intermediate and strong e-e interactions, we adopt the t-J models, treated by the Gutzwiller MF approach [97]. See more details in Appendix A. For the 30°-twisted bilayer BC_3, we adopt the small-U Hubbard model treated by the random-phase-approximation (RPA) approach [96]. See more details in Appendix B. Physically, each monolayer of these TB-QCs has been known or proposed to host SC via certain pairing mechanism, and these TB-QCs can acquire SC through the interlayer Josephson coupling. Our approach can investigate the nature of the pairing states thus obtained in the TB-QCs, including the pairing symmetry and topological properties.

III. PAIRING-SYMMETRY CLASSIFICATION

Our $\mathbf{k}$-space microscopic framework brings convenience for the pairing-symmetry classification as we can intuitively examine the distribution of the pairing gap function on the FS. Remarkably, the TB-QCs allow for more pairing-symmetry classes than crystals due to their doubly enlarged rotation groups relative to their monolayers.

The pairing symmetries are classified according to the IRRPs of the point group [98]. For a TB-QC formed by two D_n-symmetric crystalline monolayers, the point group is D_{nd}, isomorphic to D_{2n}. As listed in Table I, the D_{2n} point group has four 1D IRRPs, i.e., A_1, A_2, B_1, and B_2, and $n-1$ 2D ones E_L ($L \in [1, n-1]$). For the 1D IRRPs, the basis function of the identity representation A_1 is 1, those of B_1 and B_2 are the real and imaginary parts of $(x+iy)^n$, and their product gives that of A_2. The two basis functions of the 2D IRRP E_L are the real and imaginary parts of $(x+iy)^L$, respectively.

For each 2D IRRP E_L, the two degenerate basis gap functions would generally be mixed as $1 : \pm i$ to lower the free energy. The resultant gap function $\Delta_L^{(\pm)}(\mathbf{k})$ transform as $\Delta_L^{(\pm)}(\mathbf{k}) \to e^{\mp iL\Delta\phi}\Delta_L^{(\pm)}(\mathbf{k})$ under a $\Delta\phi = \pi/n$ rotation on the FS, corresponding to a chiral TSC with pairing angular momentum $L \leqslant n-1$. The four 1D IRRPs correspond to the

nontopological $A_{1,2}$ pairing symmetry with $L = 0$ and $B_{1,2}$ one with $L = n$. Here $L \leqslant n$ is unifiedly defined as

$$L \equiv \frac{\Delta\theta}{\Delta\phi}, \tag{8}$$

where $\Delta\theta$ represents the change of the pairing-gap phase upon every $\Delta\phi$ rotation. This pairing-symmetry classification informs us: while an n ($\leqslant 6$)-fold symmetric crystal can only carry chiral TSCs with $L \leqslant n/2 - 1 \leqslant 2$, the TB-QC can host chiral TSCs with $L = 1, \ldots, 5$ among which $L \geqslant 3$ leads to novel HAM TSCs absent in conventional crystalline materials.

The point groups relevant to the three examples studied here include the D_{12} and D_8. Concretely, the 30°-twisted bilayer graphene and the 30°-twisted bilayer BC_3 host the D_{6d} isomorphic to D_{12} and the 45°-twisted bilayer cuprates hosts the D_{4d} isomorphic to D_8. For D_{12}, the 1D IRRPs include the A_1 (s-wave, $L = 0$), the A_2 ($i*i'$, $L = 0$), the B_1, B_2 (i and i', $L = 6$); and the 2D IRRPs include the E_L ($L = 1, \ldots, 5$) (p, d, f, g, h). For D_8, the 1D IRRPs include the A_1 (s-wave, $L = 0$), the A_2 ($g*g'$, $L = 0$), the B_1, B_2 (g and g', $L = 4$); and the 2D IRRPs include the E_L ($L = 1, 2, 3$) (p, d, f).

The pairing-symmetry classification in the TB-QC is also fundamentally different from that in the intrinsic QC. Here each $|\widetilde{\mathbf{k}\alpha^{(\mu)}}\rangle$ pairs with $|\widetilde{-\mathbf{k}\alpha^{(\mu)}}\rangle$. Therefore, for a spin- singlet (triplet) pairing, the Pauli's exclusion principle requires that the pairing gap function $\Delta_{\mu\alpha}(\mathbf{k})$ should be even (odd), corresponding to even (odd) L. However, on the intrinsic QC, due to complete loss of translation symmetry, whether L is even or odd is independent from the spin statistics [26]. The reason lies in that the Pauli's principle only relates the spin statistics to the center-of-mass angular momentum of the Cooper pair, instead of the L relative to the fixed coordinate origin. Only the latter labels the pairing-symmetry classes in the intrinsic QC.

IV. THREE EXAMPLES

In this section, we provide the results of our systematic microscopic calculations for three exemplar TB-QC systems, including the 30°-twisted bilayer graphene, the 30°-twisted bilayer BC_3 and the 45°-twisted bilayer cuprates. It will be seen that novel $g + ig$, $h + ih$, and $d + id$ TSCs with HAM $L = 4, 5, 2$ would emerge in these systems.

A. The 30°-twisted bilayer graphene

The first example is the 30°-twisted bilayer graphene. It has been long to search for SC in the graphene family. Previously, the chiral $d + id$ TSC has been proposed in the mono-layer graphene [99–107], driven by e-e interaction near the van Hove (VH) doping. Recently, this material has been successfully doped to the beyond-VH regime [108], which puts on the agenda the search for the exotic $d + id$ chiral TSC. Meanwhile, the 30°-twisted bilayer graphene has been synthesized recently, whose dodecagonal symmetric QC structure has been verified by various experiments [82–86]. It's timely now to investigate what exotic pairing states can be induced by the interlayer Josephson coupling in this TB-QC.

For this TB-QC, both the intralayer and interlayer hopping integrals are provided by Eq. (2), with the related parameters given by $a \approx 0.142$ nm, $d \approx 0.335$ nm, $t_\pi \approx 2.7$ eV, $t_\sigma \approx -0.48$ eV, and $r_0 \approx 0.0453$ nm. These band-structure parameters are taken from Ref. [89]. We adopt the following t-J model Hamiltonian for this intermediate-correlated system,

$$H = H_{\mathrm{TB}} + H_J = -\sum_{\mathbf{ij}\sigma} t_{\mathbf{ij}} c^\dagger_{\mathbf{i}\sigma} c_{\mathbf{j}\sigma} + \sum_{\mathbf{i,j}} J_{\mathbf{ij}} \mathbf{S_i} \cdot \mathbf{S_j}, \tag{9}$$

with $J_{\mathbf{ij}} = 4t^2_{\mathbf{ij}}/U$. The interaction parameter $U = 10$ eV is taken from Ref. [109]. Note that the no-double-occupance constraint has been imposed on the Hilbert space of this model. We use the Gutzwiller MF approach to solve this model, see Appendix A.

The band structure of the 30°-twisted bilayer graphene (solid) is shown in Fig. 2(a) along the high-symmetric lines in the Brillouin zone (BZ), in comparison with the uncoupled band structures (dashed) from the two separate layers. The FSs for the electron doping $\delta = 0.32$ are shown in Fig. 2(b). Obviously, there are band and FS splitting induced by the interlayer hybridization, as displayed in the insets of Figs. 2(a) and 2(b). Intriguingly, the two sextuple-symmetric FSs from the two separate layers cross on the Γ-X lines and are split by the interlayer hybridization into two dodecagonal-symmetric FSs, i.e., the inner and outer pockets, with each FS containing equal components from both layers. Such fascinating dodecagonal symmetric FSs are forbidden in crystals.

Figure 2(c) shows the doping δ dependence of the pairing eigenvalue λ for the four leading pairing symmetries in the experiment-relevant doping regime $\delta \in (0, 0.4)$, with the VHS regime near $\delta_{\mathrm{v}} = \frac{1}{4}$ excluded, as the divergent DOS there might have led to other instabilities. Figure 2(c) shows that due to the FS-topology change across the VHS, the leading pairing symmetry changes from the degenerate $(d_{x^2-y^2}, d_{xy})$-wave beneath δ_{v} to the degnerate $(g_{x^4+y^4-6x^2y^2}, g_{x^3y-xy^3})$-wave beyond δ_{v}. The distributions of the degenerate d-wave and g-wave pairing gap functions on the two Fermi pockets are shown in Fig. S2 in Ref. [110].

The two components of the d- or g-wave pairings are mixed as $1 : e^{i\theta}$, and consequently the ground-state energies shown in Fig. 2(d) are minimized at $\theta = \pm\pi/2$, leading to fully-gapped $d_{x^2-y^2} \pm id_{xy}$ ($d + id$) or $g_{x^4+y^4-6x^2y^2} \pm ig_{x^3y-xy^3}$ ($g + ig$) TSCs. The distributions of their gap phases on the dodecagonal-symmetric inner pocket are shown in Figs. 2(e) and 2(f), and those on the outer pocket are provided in Fig. S3 in Ref. [110]. Clearly, the pattern in (e) ((f)) for the $d + id$ ($g + ig$) is twofold (fourfold) rotation symmetric reflecting the pairing angular momentum $L = 2$ ($L = 4$), because from Eq. (8), upon every $2\pi/L$ symmetric rotation, the change of the pairing-gap phase would accumulate to 2π. The pattern exhibited in (e) or (f) yields the winding number $W = 2$ or $W = 4$. The $g + ig$ TSC with $L = 4$ belongs to E_4 IRRP of D_{12}, which is a novel HAM TSC absent in conventional crystalline materials, because the point groups of periodic lattices only have E_1 and E_2 IRRPs, supporting the $p + ip$ ($L = 1$) and $d + id$ ($L = 2$) TSCs.

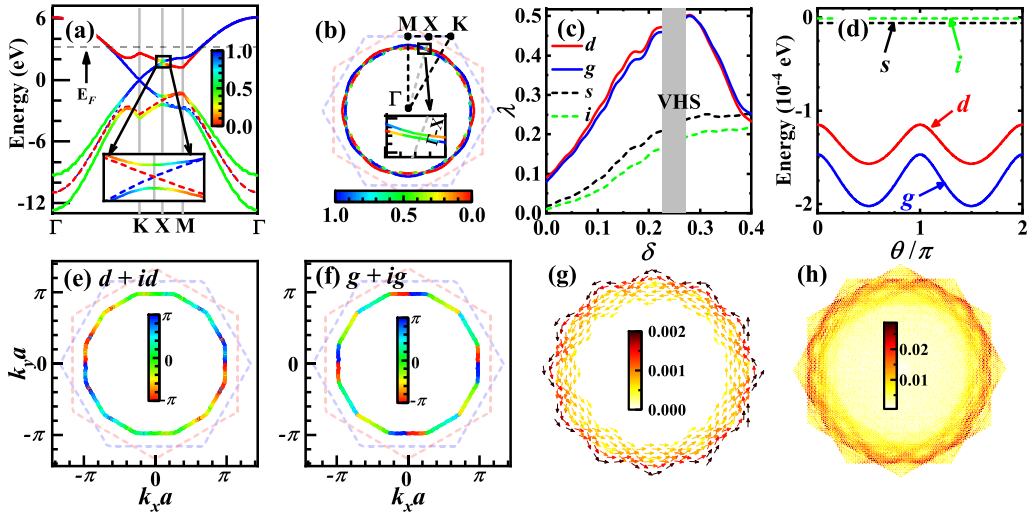

FIG. 2. Results for the 30°-twisted bilayer graphene. (a) Band structure along the high-symmetry lines: solid (dashed) lines for the coupled bilayer (two uncoupled monolayers). (b) FSs for $\delta = 0.32$ electron doping. The colors in (a) and (b) represent layer component. Inset in (a): band structure near the X point and that in (b): FSs crossing the Γ-X line (grey solid). (c) The $\lambda \sim \delta$ relations for the four leading pairing symmetries, with the VHS regime (grey) excluded. (d) Mixing-phase-angle θ dependencies of the energies for the degenerate d- and g-wave pairings. The energies of the s- and i-wave pairings are also shown in comparison. The distributions of the gap phases for the $d + id$- (e) and the $g + ig$- (f) TSCs on the inner Fermi pocket. The real-space distributions of the spontaneous super current (g) and a typical Majorana zero mode (h). In (g), the color and orientation of the arrows indicate the amplitude and direction of the super current. The doping level for (d)–(h) is $\delta = 0.32$.

B. The 30°-twisted bilayer BC_3

The second example is the 30°-twisted bilayer BC_3. The BC_3 is a D_6-symmetric genuine 2D material already synthesized [111]. While the undoped BC_3 is a band insulator, it can be electron-doped through chemical absorption with lithium adatoms. The low-energy DFT band structure of electron-doped BC_3 is well fitted by a single Boron-p_z-orbital TB model on the honeycomb lattice [112]. Remarkably, at the critical filling fraction $\delta_v \sim 1/2$ for the lower band, its FS goes through a Lifshitz transition at which it has six saddle points $\mathbf{k}_v$ satisfying $\mathbf{k}_v \neq -\mathbf{k}_v$, as shown in Fig. 3(a), forming the type-II VH singularity (VHS) [113]. The combined renormalization-group and RPA approaches predict $p + ip$ TSC near δ_v via the Kohn-Luttinger pairing mechanism [112]. Now it's interesting to investigate the pairing states induced by interlayer Josephson coupling in this TB-QC.

For this TB-QC, the intralayer hopping integrals are provided by Ref. [112], including the nearest-neighbor (NN) hopping intergal $t_1 = -0.62$ eV, the next-nearest-neighbor (NNN) one $t_2 = 0$, and the next-next-nearest-neighbor (NNNN) one $t_3 = 0.38$ eV. The interlayer hopping integrals take the formula of Eq. (2), with the related parameters given by $a \approx 0.297$ nm [111], $d \approx 0.7$ nm, $t_\pi = -0.62$ eV, $t_\sigma = 0.1$ eV, and $r_0 = 0.095$ nm, respectively. We adopt the following weak-U Hubbard model,

$$H = H_{\mathrm{TB}} + U \sum_{\mathbf{i}} n_{\mathbf{i}\uparrow} n_{\mathbf{i}\downarrow}, \tag{10}$$

with the repulsive interaction $U = 0.5$ eV [112]. This model is solved by the RPA approach, see Appendix B.

The band structure and FSs of this material provided in Fig. S4 in Ref. [110] illustrate similar splitting caused by

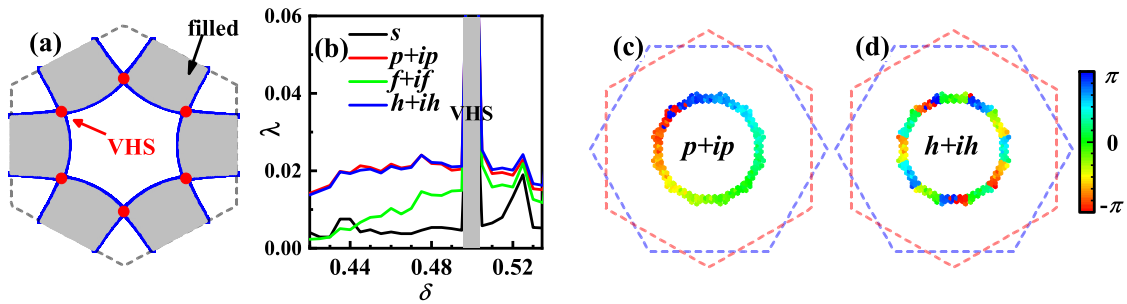

FIG. 3. Results for the 30°-twisted bilayer BC_3. (a) FSs of the monolayer BC_3 doped to its type-II VHS at $\delta_v \sim \frac{1}{2}$. The grey-colored regime is filled. (b) The $\lambda \sim \delta$ relations for the four leading pairing symmetries around the VHS regime (grey). The distributions of the gap phases for the $p + ip$- (c) and the $h + ih$- (d) TSCs on the inner Fermi pocket.

interlayer hybridization. The point group and pairing-symmetry classification of this material are identical with those of the 30°-twisted bilayer graphene. The $\lambda \sim \delta$ relations shown in Fig. 3(b) shows that the leading pairing symmetry around δ_v is the $h + ih$, with the $p + ip$ to be a close competitor which can also be the leading one away from δ_v. The distributions of their gap phases on the inner pocket are shown in Figs. 3(c) and 3(d), and those on the outer pocket are given in Fig. S5 in Ref. [110]. Clearly, the change of the pairing-gap phase of $p + ip$ shown in Fig. 3(c) accumulates to 2π for each run on the FS, leading to the winding number $W = 1$. Note that since $2\pi/5$ is not a symmetry rotation of the lattice, the pattern in (d) is not exactly fivefold rotation symmetric. However, the winding number $W = 5$ for the $h + ih$ TSC is clearly visible. The $h + ih$ TSC with $L = 5$ belongs to E_5 IRRP of the D_{12} point group, which is also a novel HAM TSC absent in crystals.

C. The 45°-twisted bilayer cuprates

The third example is the 45°-twisted bilayer cuprates. The DFT calculations predicted the stability of this structure [114], which was recently experimentally fabricated, and definite evidences for coherent interlayer Josephson tunneling were detected [87,88]. In the theoretical aspect, although the G-L theory has predicted $d + id$ TSC in this system [114–116], more information on the pairing state, such as the Chern number, should be determined by microscopic calculations. Presently, such microscopic calculations are limited to commensurate twisted angles. For general twisted angles, particularly the exact 45°, our perturbational-band theory based microscopic framework applies.

For this TB-QC, the hopping integrals appearing in Eq. (1) are set as follow. For the intralayer hopping integrals, we only keep the NN one set as $t_1 = 0.2$ eV and the NNN one set as $t_2 = -0.2t_1$. For the interlayer hopping integrals, we take the formula of Eq. (2), with the related parameters given by $a \approx 0.54$ nm, $d \approx 1.2$ nm, $t_\pi \approx 0.68$ eV, $t_\sigma \approx 30$ meV, and $r_0 \approx 0.211$ nm. The interlayer hopping integrals $\{t_{ij}\}$ thus obtained are exactly the same as those given in Ref. [114]. We adopt the same t-J model as Eq. (9), with the super exchange interaction coefficients set as $J_{ij} = 4t_{ij}^2/U$. Here $U = 2$ eV is the charge-transfer energy between the Cu-3d orbitals and the O-2p orbitals. This model is solved by the Gutzwiller MF approach.

The band structure and the octagonal-symmetric FSs have been shown in Figs. 1(c) and 1(d). The $T_c \sim \delta$ relations for various pairing symmetries belonging to the D_8 IRRPs shown in Fig. 4(a) suggests that the degenerate $(d_{x^2-y^2}, d_{xy})$ doublets are the leading one, which are further mixed as $1 : \pm i$ to lower the energy, forming the fully gapped $d + id$ TSC. The distribution of its gap phase on the inner pocket shown in Fig. 4(b) is twofold rotation symmetric, exhibits a winding number 2, so does that on the outer pocket shown in Fig. S6(f) in Ref. [110]. It's interesting that, starting from the nontopological d-wave pairing in each monolayer, we arrive at the $d + id$ TSC in the corresponding TB-QC.

More details of the results for the above three examples are provided in Ref. [110]. These HAM TSCs can be identified by phase sensitive experiments [117], see Fig. S7 in Ref. [110].

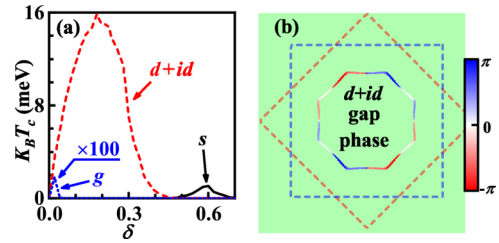

FIG. 4. Results for the 45°-twisted bilayer cuprates. (a) Doping dependence of the T_c of the three leading pairing symmetries for the hole doping, with that for the g-wave enlarged by 100 to enhance the visibility. (b) The distribution of the gap phase of the obtained $d + id$-wave pairing on the inner pocket.

V. TOPOLOGICAL PROPERTIES

Our **k**-space microscopic framework possesses clear advantages over the real-space approaches in the study of the topological properties of TSCs in extrinsic QCs. In the weak pairing limit which applies to most superconductors, the Chern number for a fully-gapped pairing state equals the sum of the pairing-phase winding numbers around all electron pockets minus that around all hole pockets [118,119]. In our first example, the distributions of the gap phases of the obtained $d + id$ and $g + ig$ TSCs on the inner pocket shown in Figs. 2(e) and 2(f) exhibit patterns characterized by the winding numbers 2 and 4, respectively. The gap functions for the two states on the outer pocket shown in the Fig. S3 in Ref. [110] exhibit the same winding numbers. Hence the Chern numbers of the $d + id$- and $g + ig$- TSC states are 4 and 8, respectively. The Chern numbers of the obtained TSC states in the remaining two examples can be obtained similarly.

The HAM TSCs obtained in the TB-QCs are novel because they not only belong to new IRRPs of the point groups, but also usually carry high Chern numbers which are rare in conventional crystalline materials. For examples, the Chern numbers of the obtained $g + ig$ or $h + ih$ TSCs in the first or second examples are 8 or 10, respectively, which are higher than the sum of the Chern numbers of the $d + id$ or $p + ip$ pairing states in the two separate layers. This change of the Chern number is caused by the FS reconstruction induced by the interlayer hybridization. For example, the FS of the 30°-twisted bilayer graphene is shown in Fig. 2(b) for the doping $\delta = 0.32$. While each separate monolayer hosts one pocket around the Γ point, the Fermi pockets from the two separate layers cross and are split by the interlayer hybridization into the inner and outer pockets. Such FS reconstruction brings chance to change the pairing-phase winding number on the FSs and hence the Chern number.

The difference between the topological properties of the TSCs on extrinsic and intrinsic QCs is clarified here. It's illustrated in Ref. [26] that in the Penrose intrinsic QC, the lack of translational symmetry causes spontaneous bulk super current in chiral TSCs. However, as shown in Fig. 2(g) for the chiral $g + ig$ TSC obtained with open boundary condition, the current only distributes at the edge with chiral pattern. Physically, the bulk current vanishes in the case of intraband pairing between opposite momenta, caused by the nearly translation symmetry here. Similarly, the Majorana zero modes are also

localized at the edge, as shown in Fig. 2(h). These topological properties make the TSCs on extrinsic QCs different from those on intrinsic QCs.

VI. DISCUSSIONS AND CONCLUSION

In conclusion, we have established an efficient microscopic framework in the **k** space to study e-e interaction driven properties of the TB-QC, based on our revised version of the perturbational-band theory. The advantage of this framework lies in that the presence of the well-defined FS brings convenience and intuition to analyze the low-energy physics in this kind of extrinsic QCs. Remarkably, the FS of the TB-QC can exhibit rotation symmetries absent in conventional crystals, such as the octagonal or dodecagonal symmetry. Moreover, the enlarged rotation symmetries in the TB-QCs allow for more pairing-symmetry classes, among which the TSCs with HAM $L \geqslant 3$ are novel TSCs absent in conventional crystalline materials. The pairing-symmetry classification and the topological properties of the pairing states in this kind of QC are also different from those in intrinsic QCs. Therefore, due to its special structure, the physical properties of the extrinsic QCs sit in between those of the crystals and the intrinsic QCs.

Note that on periodic lattices, HAM TSCs can also emerge as the higher-harmonics basis function of a given IRRP [72]. However, in such cases it would generally be strongly mixed with the low-angular-momentum one belonging to the same IRRP, unless the mixing weight of the latter happens to be very small, which is rare. Here our obtained HAM TSC is protected by the QC symmetry not to mix with other pairing states.

Our microscopic framework also applies to arbitrary large twist angle involving e-e interactions. For example, we have adopted it to study the three examples in our work and found that the pairing gap functions and topological properties of the obtained HAM TSCs are robust against slight deviation of the twist angle from the largest one. Particularly, for the twisted bilayer cuprates, when the twisted angle slightly deviates from 45°, our resultant Chern number is still 4. This result is consistent with Ref. [114] with corresponding parameters.

Our microscopic framework can also be used to study other instabilities. One example is the spin density wave (SDW) in the VH-doped 30°-twisted bilayer graphene induced by the weak coupling between the chiral SDW orders [105] in the two monolayers. Furthermore, since our approach is fully microscopic, we can use it to control electron phases through tuning such parameters as the interlayer coupling or the displacement field, to achieve more exotic phases.

ACKNOWLEDGMENTS

This work is supported by the National Natural Science Foundation of China under the Grant Nos. 12074031, 12074037, 11674025, and 12141402. W.-Q. Chen is supported by the Science, Technology and Innovation Commission of Shenzhen Municipality (No. ZDSYS20190902092905285), Guangdong Basic and Applied Basic Research Foundation under Grant No. 2020B1515120100 and Center for Computational Science and Engineering of Southern University of Science and Technology, and the National Key R&D Program of China (Grants No. 2022YFA1403700).

APPENDIX A: GUTZWILLER-MF FOR THE *t-J* MODEL

The t-J models in the 30°-twisted bilayer graphene and the 45°-twisted bilayer cuprates are studied by the following Gutzwiller mean-field (MF) [97] approach.

The Hamiltonian of the t-J model reads

$$H = -\sum_{\mathbf{ij}\sigma} t_{\mathbf{ij}} c^{\dagger}_{\mathbf{i}\sigma} c_{\mathbf{j}\sigma} + \sum_{\mathbf{i},\mathbf{j}} J_{\mathbf{ij}} \mathbf{S_i} \cdot \mathbf{S_j}, \tag{A1}$$

with $J_{\mathbf{ij}} = 4t^2_{\mathbf{ij}}/U$. The parameters U for the two systems will be presented in the SI. Here the no-double-occupance (or no-hole-occupance for the electron doping) constraint is imposed on the Hilbert space. In the Gutzwiller-MF treatment [97], such constraint can be reflected by renormalizing the hopping integral by the doping δ,

$$H_{\text{G-TB}} = -\delta \sum_{\mathbf{ij}\sigma} t_{\mathbf{ij}} c^{\dagger}_{\mathbf{i}\sigma} c_{\mathbf{j}\sigma} = \delta \sum_{\mathbf{k}\mu\alpha\sigma} \tilde{\varepsilon}^{\mu\alpha}_{\mathbf{k}} \tilde{c}^{\dagger}_{\mathbf{k}\mu\alpha\sigma} \tilde{c}_{\mathbf{k}\mu\alpha\sigma}. \tag{A2}$$

As the AFM superexchange interaction in the t-J model favors spin-singlet pairings, we reorganize it as

$$H_J = \sum_{(\mathbf{i},\mathbf{j})} J_{\mathbf{ij}} \mathbf{S_i} \cdot \mathbf{S_j} \to -\frac{3}{4} \sum_{(\mathbf{i},\mathbf{j})} J_{\mathbf{ij}} \Delta^{\dagger}_{\mathbf{ij}(0,0)} \Delta_{\mathbf{ij}(0,0)},$$
$$\Delta_{\mathbf{ij}(0,0)} = \frac{1}{\sqrt{2}} (c_{\mathbf{i}\uparrow} c_{\mathbf{j}\downarrow} - c_{\mathbf{i}\downarrow} c_{\mathbf{j}\uparrow}). \tag{A3}$$

This interaction can be transformed to the $\{|\widetilde{\mathbf{k}\alpha^{(\mu)}}\rangle\}$ bases to get the following BCS Hamiltonian:

$$H^{(\text{eff})} = \frac{1}{N} \sum_{\substack{\mathbf{k}\mu\alpha \\ \mathbf{q}\nu\beta}} \tilde{c}^{\dagger}_{\mathbf{k}\mu\alpha\downarrow} \tilde{c}^{\dagger}_{-\mathbf{k}\mu\alpha\uparrow} \tilde{c}_{-\mathbf{q}\nu\beta\uparrow} \tilde{c}_{\mathbf{q}\nu\beta\downarrow} V^{\mu\nu}_{\alpha\beta}(\mathbf{k}, \mathbf{q}),$$
$$V^{\mu\nu}_{\alpha\beta}(\mathbf{k}, \mathbf{q}) = \frac{-3}{2N} \sum_{(\mathbf{i},\mathbf{j})} J_{\mathbf{ij}} \mathbf{Re}(\tilde{\xi}_{\mathbf{i},\mathbf{k}\mu\alpha} \tilde{\xi}^{*}_{\mathbf{j},\mathbf{k}\mu\alpha}) \mathbf{Re}(\tilde{\xi}_{\mathbf{i},\mathbf{q}\nu\beta} \tilde{\xi}^{*}_{\mathbf{j},\mathbf{q}\nu\beta}). \tag{A4}$$

Here $(\tilde{\xi}_{\mathbf{k}\mu\alpha})$ represents the wave function of the state $|\widetilde{\mathbf{k}\alpha^{(\mu)}}\rangle$. Here we only consider the intra-band pairing between opposite momenta and spin, i.e., the pairing between the time-reversal pair $|\widetilde{\mathbf{k}\alpha^{(\mu)}}\uparrow\rangle$ and $|\widetilde{-\mathbf{k}\alpha^{(\mu)}}\downarrow\rangle$.

Finally, MF treatment of Eq. (A4) yields the following linearized gap equation near the T_c [96],

$$\frac{-1}{(2\pi)^2} \sum_{\nu\beta} \oint dq_{\parallel} \frac{V^{\mu\nu}_{\alpha\beta}(\mathbf{k}, \mathbf{q})}{v^{\nu\beta}_F(\mathbf{q})} \Delta_{\nu\beta}(\mathbf{q})$$
$$= \delta\lambda_\delta \Delta_{\mu\alpha}(\mathbf{k}) \equiv \lambda \Delta_{\mu\alpha}(\mathbf{k}), \tag{A5}$$

where $v^{\nu\beta}_F(\mathbf{q})$ is the bare Fermi velocity and $q_{\parallel}$ denotes the component along the tangent of the FS. For each δ, the pairing symmetry is determined by the $\Delta_{\mu\alpha}(\mathbf{k})$ corresponding to the largest pairing eigenvalue λ solved for this equation. The MF pairing temperature T^* is related to λ_δ via the relation $T^* \sim e^{-1/\lambda_\delta}$. In the Gutzwiller-MF theory, as T^* reflects the MF gap Δ_{MF} which is related to the real gap Δ_{SC} via the renormalization relation $\Delta_{\text{SC}} \approx \delta\Delta_{\text{MF}}$, we have $T_c \approx \delta T^* \propto \delta e^{-1/\lambda_\delta} \propto \delta e^{-\delta/\lambda}$.

APPENDIX B: RPA FOR THE HUBBARD MODEL

The Hubbard model adopted in the study of 30°-twisted BC_3 is treated by the following RPA approach. The Hamiltonian reads

$$H = -\sum_{\mathbf{ij}\sigma} t_{\mathbf{ij}} c^{\dagger}_{\mathbf{i}\sigma} c_{\mathbf{j}\sigma} + U \sum_{\mathbf{i}} n_{\mathbf{i}\uparrow} n_{\mathbf{i}\downarrow}. \tag{B1}$$

Here $U > 0$ means repulsive interaction.

The bare susceptibility $\chi^{(0)}$ is defined as [26]

$$\begin{aligned}\chi^{(0)}_{\mathbf{i},\mathbf{j}}(i\omega_n) &= \int_0^{\beta} d\tau e^{i\omega_n \tau} \langle T_\tau c^{\dagger}_{\mathbf{i}}(\tau) c_{\mathbf{i}}(\tau) c^{\dagger}_{\mathbf{j}}(0) c_{\mathbf{j}}(0)\rangle \\ &= \frac{1}{N^2} \sum_{\substack{\mathbf{k},\mathbf{q} \\ \mu\nu\alpha\beta}} \tilde{\xi}^{*}_{\mathbf{i},\mathbf{k}\mu\alpha} \tilde{\xi}_{\mathbf{j},\mathbf{k}\mu\alpha} \tilde{\xi}_{\mathbf{i},\mathbf{q}\nu\beta} \tilde{\xi}^{*}_{\mathbf{j},\mathbf{q}\nu\beta} F^{\mathbf{q}\nu\beta}_{\mathbf{k}\mu\alpha} \\ F^{\mathbf{q}\nu\beta}_{\mathbf{k}\mu\alpha} &= \frac{n_f\left(\tilde{\varepsilon}^{\mu\alpha}_{\mathbf{k}} - \mu_c\right) - n_f\left(\tilde{\varepsilon}^{\nu\beta}_{\mathbf{q}} - \mu_c\right)}{\tilde{\varepsilon}^{\nu\beta}_{\mathbf{q}} - \tilde{\varepsilon}^{\mu\alpha}_{\mathbf{k}} + i\omega_n}. \end{aligned} \tag{B2}$$

The renormalized susceptibility χ in the RPA level reads

$$\chi = (I - U\chi^{(0)})^{-1} \chi^{(0)}. \tag{B3}$$

Here χ and $\chi^{(0)}$ are viewed as matrices, whose $(\mathbf{i}, \mathbf{j})$ elements are just $\chi_{\mathbf{i},\mathbf{j}}$ or $\chi^{(0)}_{\mathbf{i},\mathbf{j}}$. In our calculations, we have just taken the zero-frequency component of $\chi_{\mathbf{i},\mathbf{j}}$. Then, through exchanging particle-hole excitations, a cooper pair can acquire effective attraction via the real-space Kohn-Luttinger mechanism [26], leading to the following effective Hamiltonian:

$$\begin{aligned} H_{\text{RPA-eff}} = &\sum_{\mathbf{k}\mu\alpha\sigma} \tilde{\varepsilon}^{\mu\alpha}_{\mathbf{k}} \tilde{c}^{\dagger}_{\mathbf{k}\mu\alpha\sigma} \tilde{c}_{\mathbf{k}\mu\alpha\sigma} + U \sum_{\mathbf{i}} c^{\dagger}_{\mathbf{i}\uparrow} c_{\mathbf{i}\uparrow} c^{\dagger}_{\mathbf{i}\downarrow} c_{\mathbf{i}\downarrow} \\ &- \frac{U^2}{2} \sum_{\substack{\mathbf{i},\mathbf{j} \\ \sigma\sigma'}} c^{\dagger}_{\mathbf{i}\sigma} c_{\mathbf{i}\sigma'} c^{\dagger}_{\mathbf{j}\sigma'} c_{\mathbf{j}\sigma} \chi_{\mathbf{ij}}. \end{aligned} \tag{B4}$$

The following MF treatment of Eq. (B4) is parallel to that of the above t-J model. Concretely, we shall first transform this real-space Hamiltonian into the $\mathbf{k}$ space in the $\{|\widetilde{\mathbf{k}\alpha^{(\mu)}}\rangle\}$ bases. Then through a MF study, we obtain the linearized gap equation at T_c similar with Eq. (A5), with only the $V^{\mu\nu}_{\alpha\beta}(\mathbf{k}, \mathbf{q})$ replaced by

$$\begin{aligned} V^{(s)\mu\nu}_{\alpha\beta}(\mathbf{k}, \mathbf{q}) = &\frac{U}{N} \sum_{\mathbf{i}} |\tilde{\xi}_{\mathbf{i},\mathbf{k}\mu\alpha} \tilde{\xi}_{\mathbf{i},\mathbf{q}\nu\beta}|^2 + \frac{U^2}{N} \sum_{(\mathbf{i},\mathbf{j})} \chi_{\mathbf{ij}} \\ &\times \mathbf{Re}(\tilde{\xi}_{\mathbf{i},\mathbf{k}\mu\alpha} \tilde{\xi}^{*}_{\mathbf{j},\mathbf{k}\mu\alpha}) \mathbf{Re}(\tilde{\xi}_{\mathbf{i},\mathbf{q}\nu\beta} \tilde{\xi}^{*}_{\mathbf{j},\mathbf{q}\nu\beta}) \end{aligned} \tag{B5}$$

for the singlet pairing and

$$V^{(t)\mu\nu}_{\alpha\beta}(\mathbf{k}, \mathbf{q}) = \frac{-U^2}{N} \sum_{(\mathbf{i},\mathbf{j})} \chi_{\mathbf{ij}} \mathbf{Im}(\tilde{\xi}_{\mathbf{i},\mathbf{k}\mu\alpha} \tilde{\xi}^{*}_{\mathbf{j},\mathbf{k}\mu\alpha}) \mathbf{Im}(\tilde{\xi}_{\mathbf{i},\mathbf{q}\nu\beta} \tilde{\xi}^{*}_{\mathbf{j},\mathbf{q}\nu\beta}) \tag{B6}$$

for the triplet one. The leading pairing symmetry is determined by the pairing eigenvector(s) corresponding to the largest pairing eigenvalue λ, which is related to the T_c via $T_c \propto e^{-1/\lambda}$.

[1] D. Shechtman, I. Blech, and D. Gratias, and J. W. Cahn, Phys. Rev. Lett. **53**, 1951 (1984).
[2] See, A. I. Goldman and R. F. Kelton, Rev. Mod. Phys. **65**, 213 (1993), and the references there.
[3] H. Tsunetsugu, T. Fujiwara, K. Ueda, and T. Tokihiro, Phys. Rev. B **43**, 8879 (1991).
[4] H. Tsunetsugu, K. Ueda, Phys. Rev. B **43**, 8892 (1991).
[5] S. Yamamoto and T. Fujiwara, Phys. Rev. B **51**, 8841 (1995).
[6] S. Wessel, A. Jagannathan, and S. Haas, Phys. Rev. Lett. **90**, 177205 (2003).
[7] S. Takemura, N. Takemori, and A. Koga, Phys. Rev. B **91**, 165114 (2015).
[8] E. C. Andrade, A. Jagannathan, E. Miranda, M. Vojta, and V. Dobrosavljevic, Phys. Rev. Lett. **115**, 036403 (2015).
[9] Y. E. Kraus, Y. Lahini, Z. Ringel, M. Verbin, and O. Zilberberg, Phys. Rev. Lett. **109**, 106402 (2012).
[10] H. Huang and F. Liu, Phys. Rev. Lett. **121**, 126401 (2018).
[11] S. Longhi, Phys. Rev. Lett. **122**, 237601 (2019).
[12] S. Autti, V. B. Eltsov, and G. E. Volovik, Phys. Rev. Lett. **120**, 215301 (2018).
[13] K. Giergiel, A. Kuroś, and K. Sacha, Phys. Rev. B **99**, 220303(R) (2019).
[14] L.-J. Lang, X. Cai, and S. Chen, Phys. Rev. Lett. **108**, 220401 (2012).
[15] M. A. Bandres, M. C. Rechtsman, and M. Segev, Phys. Rev. X **6**, 011016 (2016).
[16] J. Hou, H. Hu, K. Sun, and C. Zhang, Phys. Rev. Lett. **120**, 060407 (2018).
[17] D. Varjas, A. Lau, K. Pöyhönen, A. R. Akhmerov, D. I. Pikulin, and I. C. Fulga, Phys. Rev. Lett. **123**, 196401 (2019).
[18] S. Spurrier and N. R. Cooper, Phys. Rev. Res. **2**, 033071 (2020).
[19] K. Kamiya, T. Takeuchi, N. Kabeya, N. Wada, T. Ishimasa, A. Ochiai, K. Deguchi, K. Imura, and N. K. Sato, Nat. Commun. **9**, 154 (2018).
[20] K. M. Wong, E. Lopdrup, J. L. Wagner, Y. Shen, and S. J. Poon, Phys. Rev. B **35**, 2494 (1987).
[21] W. DeGottardi, D. Sen, and S. Vishveshwara, Phys. Rev. Lett. **110**, 146404 (2013).
[22] I. C. Fulga, D. I. Pikulin, and T. A. Loring, Phys. Rev. Lett. **116**, 257002 (2016).
[23] S. Sakai, N. Takemori, A. Koga, and R. Arita, Phys. Rev. B **95**, 024509 (2017).
[24] R. N. Araújo and E. C. Andrade, Phys. Rev. B **100**, 014510 (2019).
[25] S. Sakai and R. Arita, Phys. Rev. Res. **1**, 022002(R) (2019).
[26] Y. Cao, Y. Zhang, Y.-B. Liu, C.-C. Liu, W.-Q. Chen, and F. Yang, Phys. Rev. Lett. **125**, 017002 (2020).
[27] Y. Nagai, J. Phys. Soc. Jpn. **89**, 074703 (2020).
[28] N. Takemori, R. Arita, and S. Sakai, Phys. Rev. B **102**, 115108 (2020).
[29] J. B. Hauck, C. Honerkamp, S. Achilles, and D. M. Kennes, Phys. Rev. Res. **3**, 023180 (2021).
[30] C.-B. Hua, Z.-R. Liu, T. Peng, R. Chen, D.-H. Xu, and B. Zhou, Phys. Rev. B **104**, 155304 (2021).

[31] Y.-B. Liu, J.-J. Hao, Y. Zhang, Y. Cao, W.-Q. Chen, and F. Yang, Sci. China Phys. Mech. Astron. **65**, 287411 (2022).

[32] S. Sakai, R. Arita, and T. Ohtsuki, Phys. Rev. B **105**, 054202 (2022).

[33] M. Khosravian and J. L. Lado, Phys. Rev. Res. **3**, 013262 (2021).

[34] E. Day-Roberts, R. M. Fernandes, and A. Kamenev, Phys. Rev. B **102**, 064210 (2020).

[35] Y. Cao, V. Fatemi, A. Demir, S. Fang, S. L. Tomarken, J. Y. Luo, J. D. Sanchez-Yamagishi, K. Watanabe, T. Taniguchi, E. Kaxiras, R. C. Ashoori, and P. Jarillo-Herrero, Nature (London) **556**, 80 (2018).

[36] Y. Cao, V. Fatemi, S. Fang, K. Watanabe, T. Taniguchi, E. Kaxiras, and P. Jarillo-Herrero, Nature (London) **556**, 43 (2018).

[37] G. Chen, A. L. Sharpe, P. Gallagher, I. T. Rosen, E. Fox, L. Jiang, B. Lyu, H. Li, K. Watanabe, T. Taniguchi *et al.*, Nature (London) **572**, 215 (2019).

[38] X. Liu, Z. Hao, E. Khalaf, J. Y. Lee, K. Watanabe, T. Taniguchi, A. Vishwanath, and P. Kim, Nature (London) **583**, 221 (2020).

[39] C. Shen, Y. Chu, Q. Wu, N. Li, S. Wang, Y. Zhao, J. Tang, J. Liu, J. Tian, K. Watanabe *et al.*, Nat. Phys. **16**, 520 (2020).

[40] J. Park, Y. Cao, K. Watanabe, T. Taniguchi, and P. Jarillo-Herrero, Nature (London) **590**, 249 (2021).

[41] L. Xian, D. M. Kennes, N. Tancogne-Dejean, M. Altarelli, and A. Rubio, Nano Lett. **19**, 4934 (2019).

[42] L. Wang, E.-M. Shih, A. Ghiotto, L. Xian, D. A. Rhodes, C. Tan, M. Claassen, D. M. Kennes, Y. Bai, B. Kim *et al.*, Nat. Mater. **19**, 861 (2020).

[43] E. C. Regan, D. Wang, C. Jin, M. I. B. Utama, B. Gao, X. Wei, S. Zhao, W. Zhao, K. Yumigeta, M. Blei *et al.*, Nature (London) **579**, 359 (2020).

[44] Y. Tang, L. Li, T. Li, Y. Xu, S. Liu, K. Barmak, K. Watanabe, T. Taniguchi, A. H. MacDonald, J. Shan, and K. F. Mak, Nature (London) **579**, 353 (2020).

[45] M. Yankowitz, S. Chen, H. Polshyn, Y. Zhang, K. Watanabe, T. Taniguchi, D. Graf, A. F. Young, and C. R. Dean, Science **363**, 1059 (2019).

[46] Y. Xie, B. Lian, B. Jäck, X. Liu, C.-L. Chiu, K. Watanabe, T. Taniguchi, B. A. Bernevig, and A. Yazdani, Nature (London) **572**, 101 (2019).

[47] X. Lu, P. Stepanov, W. Yang, M. Xie, M. A. Aamir, I. Das, C. Urgell, K. Watanabe, T. Taniguchi, G. Zhang, A. Bachtold, A. H. MacDonald, and D. K. Efetov, Nature (London) **574**, 653 (2019).

[48] A. L. Sharpe, E. J. Fox, A. W. Barnard, J. Finney, K. Watanabe, T. Taniguchi, M. A. Kastner, and D. Goldhaber-Gordon, Science **365**, 605 (2019).

[49] M. Serlin, C. L. Tschirhart, H. Polshyn, Y. Zhang, J. Zhu, K. Watanabe, T. Taniguchi, L. Balents, and A. F. Young, Science **367**, 900 (2019).

[50] A. Uri, S. Grover, Y. Cao, J. A. Crosse, K. Bagani, D. Rodan-Legrain, Y. Myasoedov, K. Watanabe, T. Taniguchi, P. Moon, M. Koshino, P. Jarillo-Herrero, and E. Zeldov, Nature (London) **581**, 47 (2020).

[51] Y. Cao, D. Rodan-Legrain, J. M. Park, N. F. Yuan, K. Watanabe, T. Taniguchi, R. M. Fernandes, L. Fu, and P. Jarillo-Herrero, Science **372**, 264 (2021).

[52] R. Bistritzer and A. H. MacDonald, Proc. Natl. Acad. Sci. USA **108**, 12233 (2011).

[53] C. Xu and L. Balents, Phys. Rev. Lett. **121**, 087001 (2018).

[54] H. C. Po, L. Zou, A. Vishwanath, and T. Senthil, Phys. Rev. X **8**, 031089 (2018).

[55] N. F. Q. Yuan and L. Fu, Phys. Rev. B **98**, 045103 (2018).

[56] C.-C. Liu, L.-D. Zhang, W.-Q. Chen, and F. Yang, Phys. Rev. Lett. **121**, 217001 (2018).

[57] F. Wu, A. H. MacDonald, and I. Martin, Phys. Rev. Lett. **121**, 257001 (2018).

[58] J. Kang and O. Vafek, Phys. Rev. X **8**, 031088 (2018); Phys. Rev. Lett. **122**, 246401 (2019).

[59] H. Isobe, N. F. Q. Yuan, and L. Fu, Phys. Rev. X **8**, 041041 (2018).

[60] M. Koshino, N. F. Q. Yuan, T. Koretsune, M. Ochi, K. Kuroki, and L. Fu, Phys. Rev. X **8**, 031087 (2018).

[61] J. W. F. Venderbos and R. M. Fernandes, Phys. Rev. B **98**, 245103 (2018).

[62] J. Liu, Z. Ma, J. Gao, and X. Dai, Phys. Rev. X **9**, 031021 (2019).

[63] J. Gonzalez and T. Stauber, Phys. Rev. Lett. **122**, 026801 (2019).

[64] Z. Song, Z. Wang, W. Shi, G. Li, C. Fang, and B. A. Bernevig, Phys. Rev. Lett. **123**, 036401 (2019).

[65] M. Angeli, E. Tosatti, and M. Fabrizio, Phys. Rev. X **9**, 041010 (2019).

[66] Y.-P. Lin and R. M. Nandkishore, Phys. Rev. B **100**, 085136 (2019); **102**, 245122 (2020).

[67] M. Xie and A. H. MacDonald, Phys. Rev. Lett. **124**, 097601 (2020).

[68] A. Abouelkomsan, Z. Liu, and E. J. Bergholtz, Phys. Rev. Lett. **124**, 106803 (2020).

[69] N. Bultinck, E. Khalaf, S. Liu, S. Chatterjee, A. Vishwanath, and M. P. Zaletel, Phys. Rev. X **10**, 031034 (2020).

[70] C. Repellin, Z. Dong, Y.-H. Zhang, and T. Senthil, Phys. Rev. Lett. **124**, 187601 (2020).

[71] Y. Da Liao, J. Kang, C. N. Breio, X. Y. Xu, H.-Q. Wu, B. M. Andersen, R. M. Fernandes, and Z. Y. Meng, Phys. Rev. X **11**, 011014 (2021).

[72] D. V. Chichinadze, L. Classen, and A. V. Chubukov, Phys. Rev. B **101**, 224513 (2020).

[73] M. Alidoust, A.-P. Jauho, and J. Akola, Phys. Rev. Res. **2**, 032074 (2020).

[74] L. Xian, M. Claassen, D. Kiese, M. M. Scherer, S. Trebst, D. M. Kennes, and A. Rubio, Nat. Commun. **12**, 5644 (2021).

[75] M. Angeli and MacDonald, Proc. Natl. Acad. Sci. USA **118**, e2021826118 (2021).

[76] M. H. Naik and M. Jain, Phys. Rev. Lett. **121**, 266401 (2018).

[77] F. Wu, T. Lovorn, E. Tutuc, and A. H. MacDonald, Phys. Rev. Lett. **121**, 026402 (2018).

[78] D. M. Kennes, M. Claassen, L. Xian, A. Georges, A. J. Millis, J. Hone, C. R. Dean, D. N. Basov, A. N. Pasupathy, and A. Rubio, Nat. Phys. **17**, 155 (2021).

[79] C. Lu, Y. Zhang, Y. Zhang, M. Zhang, C.-C. Liu, Y. Wang, Z.-C. Gu, W.-Q. Chen, and F. Yang, Phys. Rev. B **106**, 024518 (2022).

[80] M. Zhang, Y. Zhang, C. Lu, W.-Q. Chen, and F. Yang, Chin. Phys. B **29**, 127102 (2020).

[81] Y.-N. Ren, C. Lu, Y. Zhang, S.-Y. Li, Y.-W. Liu, C. Yan, Z.-H. Guo, C.-C. Liu, F. Yang, and L. He, ACS Nano **14**, 13081 (2020).
[82] S. J. Ahn, P. Moon, T. H. Kim, H. W. Kim, H. C. Shin, E. H. Kim, H. W. Cha, S. J. Kahng, P. Kim, M. Koshino *et al.*, Science **361**, 782 (2018).
[83] W. Yao, E. Wang, C. Bao, Y. Zhang, K. Zhang, K. Bao, C. K. Chan, C. Chen, J. Avila, M. C. Asensio, J. Zhu, and S. Zhou, Proc. Natl. Acad. Sci. USA **115**, 6928 (2018).
[84] C. Yan, D.-L. Ma, J.-B. Qiao, H.-Y. Zhong, L. Yang, S.-Y. Li, Z.-Q. Fu, Y. Zhang, and L. He, 2D Mater. **6**, 045041 (2019).
[85] S. Pezzini, V. Miseikis, G. Piccinini, S. Forti, S. Pace, R. Engelke, F. Rossella, K. Watanabe, T. Taniguchi, P. Kim, and C. Coletti, Nano Lett. **20**, 3313 (2020).
[86] B. Deng, B. Wang, N. Li, R. Li, Y. Wang, J. Tang, Q. Fu, Z. Tian, P. Gao, J. Xue, and H. Peng, ACS Nano **14**, 1656 (2020).
[87] Y. Zhu, M. Liao, Q. Zhang, H.-Y. Xie, F. Meng, Y. Liu, Z. Bai, S. Ji, J. Zhang, K. Jiang *et al.*, Phys. Rev. X **11**, 031011 (2021).
[88] S. Y. Frank Zhao, N. Poccia, X. Cui, P. A. Volkov, H. Yoo, R. Engelke, Y. Ronen, R. Zhong, G. Gu, S. Plugge, T. Tummuru, M. Franz, J. H. Pixley, and P. Kim, arXiv:2108.13455.
[89] P. Moon, M. Koshino, and Y.-W. Son, Phys. Rev. B **99**, 165430 (2019).
[90] M. J. Park, H. S. Kim, and S. B. Lee, Phys. Rev. B **99**, 245401 (2019).
[91] G. Yu, Z. Wu, Z. Zhan, M. I. Katsnelson, and S. Yuan, npj Comput Mater **5**, 122 (2019).
[92] G. Yu, Z. Wu, Z. Zhan, M. I. Katsnelson, and S. Yuan, Phys. Rev. B **102**, 115123 (2020).
[93] J. L. Aragon, G. G. Naumis, and A. Gomez-Rodriguez, Crystals **9**, 519 (2019).
[94] P. Moon and M. Koshino, Phys. Rev. B **87**, 205404 (2013).
[95] M. Koshino, New J. Phys. **17**, 015014 (2015).
[96] S. Graser, T. A. Maier, P. J. Hirschfeld, and D. J. Scalapino, New J. Phys. **11**, 025016 (2009).
[97] F.-C. Zhang, C. Gros, T. M. Rice, and H. Shiba, Supercond. Sci. Technol. **1**, 36 (1988).
[98] M. Sigrist and K. Ueda, Rev. Mod. Phys. **63**, 239 (1991).
[99] A. M. Black-Schaffer and S. Doniach, Phys. Rev. B **75**, 134512 (2007).
[100] J. Gonzalez, Phys. Rev. B **78**, 205431 (2008).
[101] C. Honerkamp, Phys. Rev. Lett. **100**, 146404 (2008).
[102] S. Pathak, V. B. Shenoy, and G. Baskaran, Phys. Rev. B **81**, 085431 (2010).
[103] J. L. McChesney, A. Bostwick, T. Ohta, T. Seyller, K. Horn, J. Gonzalez, and E. Rotenberg, Phys. Rev. Lett. **104**, 136803 (2010).
[104] R. Nandkishore, L. S. Levitov, and A. V. Chubukov, Nat. Phys. **8**, 158 (2012).
[105] W.-S. Wang, Y.-Y. Xiang, Q.-H. Wang, F. Wang, F. Yang, and D.-H. Lee, Phys. Rev. B **85**, 035414 (2012).
[106] M. L. Kiesel, C. Platt, W. Hanke, D. A. Abanin, and R. Thomale, Phys. Rev. B **86**, 020507 (2012).
[107] A. M. Black-Schaffer and C. Honerkamp, J. Phys.: Condens. Matter **26**, 423201 (2014).
[108] P. Rosenzweig, H. Karakachian, D. Marchenko, K. Kuster, and U. Starke, Phys. Rev. Lett. **125**, 176403 (2020).
[109] A. H. Castro Neto, F. Guinea, N. M. R. Peres, K. S. Novoselov, and A. K. Geim, Rev. Mod. Phys. **81**, 109 (2009).
[110] See Supplemental Material at http://link.aps.org/supplemental/10.1103/PhysRevB.107.014501 for more calculation results for the three examples and the description of phase sensitive experiments.
[111] H. Yanagisawa, T. Tanaka, Y. Ishida, M. Matsue, E. Rokuta, S. Otani, and C. Oshima, Phys. Rev. Lett. **93**, 177003 (2004).
[112] X. Chen, Y. Yao, H. Yao, F. Yang, and J. Ni, Phys. Rev. B **92**, 174503 (2015).
[113] H. Yao and F. Yang, Phys. Rev. B **92**, 035132 (2015).
[114] O. Can, T. Tummuru, R. P. Day, I. Elfimov, A. Damascelli, and M. Franz, Nat. Phys. **17**, 519 (2021).
[115] Z. Yang, S. Qin, Q. Zhang, C. Fang, and J. Hu, Phys. Rev. B **98**, 104515 (2018).
[116] A. Mercado, S. Sahoo, and M. Franz, Phys. Rev. Lett. **128**, 137002 (2022).
[117] D. J. Van Harlingen, Rev. Mod. Phys. **67**, 515 (1995).
[118] X.-L. Qi, T. L. Hughes, and S.-C. Zhang, Phys. Rev. B **82**, 184516 (2010).
[119] J. Alicea, Rep. Prog. Phys. **75**, 076501 (2012).